On simulations of discrete fracture network flows with an optimization-based extended finite element method — Source link

Stefano Berrone, Sandra Pieraccini, Stefano Scialò

Topics: Extended finite element method, Discretization, Finite element method, Flow network and Fracture (geology)

Related papers:

- A PDE-Constrained Optimization Formulation for Discrete Fracture Network Flows

- An optimization approach for large scale simulations of discrete fracture network flows

- The virtual element method for discrete fracture network simulations

- A Generalized Mixed Hybrid Mortar Method for Solving Flow in Stochastic Discrete Fracture Networks

- Modeling Fractures and Barriers as Interfaces for Flow in Porous Media

On simulations of discrete fracture network flows with an optimization-based extended finite element method

(Article begins on next page)

30 May 2022

ON SIMULATIONS OF DISCRETE FRACTURE NETWORK FLOWS WITH AN OPTIMIZATION-BASED EXTENDED FINITE ELEMENT METHOD[*]

STEFANO BERRONE[†], SANDRA PIERACCINI[†], AND STEFANO SCIALÒ[†]

Abstract. Following the approach introduced in [*SIAM J. Sci. Comput.*, 35 (2013), pp. B487–B510], we consider the formulation of the problem of fluid flow in a system of fractures as a PDE constrained optimization problem, with discretization performed using suitable extended finite elements; the method allows independent meshes on each fracture, thus completely circumventing meshing problems usually related to the discrete fracture network (DFN) approach. The application of the method to DFNs of medium complexity is fully analyzed here, accounting for several issues related to viable and reliable implementations of the method in complex problems.

Key words. fracture flows, Darcy flows, discrete fracture networks, optimization methods for elliptic problems

AMS subject classifications. 65N30, 65N15, 65N50, 65J15

DOI. 10.1137/120882883

1. Introduction. In many applications, such as water resources monitoring, contaminant transport, and oil/gas recovery, efficient numerical simulations of subsurface fluid flow in fractured porous rocks are of increasing interest. The description of the phenomena has to correctly account for the intrinsic heterogeneity and directionality of the rock medium and the multiscale nature of the flow. In dense fracture networks the flow can be well modeled as the flow in a continuous porous medium where fractures influence the distribution of an equivalent permeability tensor. On the contrary, in sparse fracture networks flow properties are mainly determined by the larger fractures; thus discrete fracture network (DFN) models are preferred to more conventional continuum models as basis for the simulations.

A DFN is an assemblage of resembling-fractures planar ellipses or polygons, stochastically generated given probabilistic data on distribution of density, aspect ratio, orientation, size, aperture, and hydrological properties of the medium [12]. The fluid regime in a DFN can be conditioned even by the smallest elements, and therefore neglecting fractures below a specified threshold is not recommended. As a consequence the number of generated fractures is frequently high even for a limited size of the domain of interest. Discretization thus often leads to poor meshes with a huge number of nodes. At the same time, a stochastic approach to the uncertainty of the parameters requires large numbers of simulations so that efficiency of numerical methods is of paramount importance for the applicability of DFN-based numerical solutions.

A DFN is a complex three-dimensional (3D) structure. The first numerical challenge is to provide good-quality conforming meshes where the discretization of fracture intersections (*traces*) is the same on all the fractures involved. This is usually achieved by the introduction of a huge number of elements, independently of the required accuracy of the numerical solution.

[†]Dipartimento di Scienze Matematiche, Politecnico di Torino, Corso Duca degli Abruzzi 24, 10129 Torino, Italy (stefano.berrone@polito.it, sandra.pieraccini@polito.it, stefano.scialo@polito.it).

In order to reduce computational cost, a possible approach consists in reducing the DFNs to systems of one-dimensional pipes that are aligned along the fractures and mutually connect the centers of the traces with the surrounding fractures. This approach eases mesh generation problems and the resulting mesh of pipes still reflects the topological properties of the fracture network [8, 23]. An accurate definition of pipe properties is obtained with a boundary element method in [13].

Without resorting to dimensionality reduction, in [30] a mixed nonconforming finite element method on a conforming mesh is proposed. In [21], an adaptive approach to the conforming mesh generation requiring adjustments of the trace spatial collocations is proposed. Local modifications of the mesh or of the fracture network in order to preserve conformity of the meshes or alignment of meshes along the traces are considered in several works (see, e.g., [18, 30]). In [15], a method to generate a good-quality conforming mesh on the network system is proposed based on the projection of the discrete 3D network on the two-dimensional planar fractures in order to remove those connections among fractures which are difficult to be meshed. In [25, 26], a mixed hybrid mortar method is proposed allowing nonconformities of the meshes on the fractures but requiring that the traces are contained in the set of the edges of each fracture triangulation. Resorting to mortar methods, the discretization of each fracture can lead to a different discretization of the traces. Interesting, very complex DFN configurations are tested in [14].

In the recent work [6], the authors have proposed a different approach for the description of steady-state flows in a given DFN, which consists in the reformulation of the problem as a PDE constrained optimization problem. Following this approach, it is shown that the meshes introduced on each fracture are allowed to be independent of the meshes on other fractures and independent of trace number and disposition, thus actually eliminating any kind of meshing problems related to DFN. The discrete problem is formulated as an equality constrained quadratic programming problem. Discretization on each fracture is performed with the extended finite element method (XFEM) for approximating the nonsmooth behavior of the solution, which may present discontinuities in the fluxes. Here, we further analyze viability of the method proposed in [6] by discussing several issues arising when the method is applied to complex DFNs. In particular, we fully account for the extended finite element discretization with the so-called open interfaces, i.e., traces not ending on fracture edges. We also discuss preconditioning issues related to the numerical solution of the problem. Several numerical results are proposed, showing the capability of the method in dealing with complex situations, such as critical traces intersections.

The paper is organized as follows. In section 2 we briefly recall the physical model and the continuous optimization problem, and in section 3 the discrete formulation of the problem is given. In section 4 we describe the basics of extended finite elements considered herein, with special attention given to the treatment of open interfaces. In section 5 numerical results are discussed in order to prove viability and reliability of the method.

2. Problem description. The quantity of interest of the problem we are dealing with is the hydraulic head, given by $H = \mathcal{P} + \zeta$, where $\mathcal{P} = p/(\varrho g)$ is the pressure head, p is the fluid pressure, g is the gravitational acceleration constant, ϱ is the fluid density, and ζ is the elevation. The computation of the hydraulic head in a DFN requires the solution of differential equations on a system of planar polygonal open sets called fractures, denoted by F_i with $i \in \mathfrak{I}$. Let us introduce on each F_i a local tangential coordinate system $\hat{x}_i$. Despite being planar, their orientations typically

differ so that their union is a 3D set. Let us denote by Ω the union of the fractures and let $\partial\Omega$ be its boundary. The intersection of the closure of each couple of fractures is either an empty set or a set of nonvanishing segments called *traces*, denoted by S_m, $m \in \mathfrak{M}$. Let $\mathcal{S}$ denote the set of all these traces. Furthermore, let each fracture of the system be endowed with a hydraulic transmissivity tensor $\mathbf{K}_i(\hat{x}_i)$.

In this paper the following assumptions are made on the DFN: (1) $\bar{\Omega}$ is a connected set; (2) each trace S_m, $m \in \mathfrak{M}$, is shared by exactly two polygonal fractures F_i and F_j, $i \neq j$: $S_m \subseteq \bar{F}_i \cap \bar{F}_j$; (3) on each fracture, the transmissivity tensor $\mathbf{K}_i(\hat{x}_i)$ is symmetric and uniformly positive definite.

Given a trace S_m, let F_i and F_j be the fractures sharing the trace: the set of indices i and j is denoted by $I_{S_m} = \{i,j\}$. For each fracture F_i let us denote by $\mathcal{S}_i$ the set of traces shared by F_i with other fractures and by $J_i \subset \mathfrak{I}$ the set of indices of fractures sharing one trace with F_i.

While referring the reader to [6] for all the details, we sketch here a brief description of the approach. Let us split the boundary $\partial\Omega$ into two sets $\Gamma_D \neq \emptyset$ and Γ_N with $\Gamma_D \cup \Gamma_N = \partial\Omega$ and $\Gamma_D \cap \Gamma_N = \emptyset$, on which Dirichlet boundary conditions H_D and Neumann boundary conditions G_N are respectively imposed. Let H_{iD} and G_{iN} be the restriction of H_D and G_N to $\Gamma_{iD} = \Gamma_D \cap \partial F_i$ and $\Gamma_{iN} = \Gamma_N \cap \partial F_i$, respectively. Let us define $\forall i \in \mathfrak{I}$

$$V_i = \mathrm{H}_0^1(F_i) = \left\{ v \in \mathrm{H}^1(F_i) : v_{|\Gamma_{iD}} = 0 \right\}, \ V_i^D = \mathrm{H}_\mathrm{D}^1(F_i) = \left\{ v \in \mathrm{H}^1(F_i) : v_{|\Gamma_{iD}} = H_{iD} \right\},$$

and let V_i' be the dual space of V_i.

The global hydraulic head H in the whole connected system Ω is provided by the solution of the following problems: $\forall i \in \mathfrak{I}$ find $H_i \in V_i^D$ such that $\forall v \in V_i$

$$(2.1) \quad \int_{F_i} \mathbf{K}_i \nabla H \nabla v \mathrm{d}\Omega = \int_{F_i} q_i v \mathrm{d}\Omega + \int_{\Gamma_N \cap \partial F_i} G_{i,N} v_{|S} \mathrm{d}\Gamma + \sum_{S \in \mathcal{S}_i} \int_S \left[\!\left[\frac{\partial H_i}{\partial \hat{\nu}_S^i} \right]\!\right]_{S_m} v_{|S} \mathrm{d}\Gamma,$$

where $\frac{\partial H_i}{\partial \hat{\nu}_S^i} = (\hat{n}_S^i)^T \mathbf{K} \nabla H$ is the outward co-normal derivative of the hydraulic head, where $\hat{n}_S^i$ is the unique normal fixed for the trace S on the fracture F_i, and the symbol $[\![\frac{\partial H_i}{\partial \hat{\nu}_S^i}]\!]_S$ denotes the jump of the co-normal derivative along $\hat{n}_S^i$. This jump is independent of the orientation of $\hat{n}_S^i$.

In (2.1) the left-hand side models the diffusion of hydraulic head on each fracture, the first term of the right-hand side is the external load in each facture, the second is the term due to the Neumann boundary conditions, and the last term describes the net flow of hydraulic head entering the fracture at each trace.

In order to set up a well-defined problem, the following matching conditions have to be added to (2.1):

$$(2.2) \quad H_{i|S_m} - H_{j|S_m} = 0 \qquad \text{for } i,j \in I_{S_m},$$

$$(2.3) \quad \left[\!\left[\frac{\partial H_i}{\partial \hat{\nu}_{S_m}^i} \right]\!\right]_{S_m} + \left[\!\left[\frac{\partial H_j}{\partial \hat{\nu}_{S_m}^j} \right]\!\right]_{S_m} = 0 \qquad \text{for } i,j \in I_{S_m}.$$

These two additional conditions correspond to the physical requirement of continuity of the hydraulic head and conservation of hydraulic fluxes across each trace S_m, $m \in \mathfrak{M}$. Condition (2.2) implies that the hydraulic head H on the whole domain Ω belongs to the space

$$(2.4) \quad V^D = \mathrm{H}^1_{\mathrm{D}}(\Omega) = \left\{ v \in \prod_{i \in \mathfrak{I}} V_i^D : (v_{|_{F_i}})_{|_{S_m}} = (v_{|_{F_j}})_{|_{S_m}}, \ i,j \in I_{S_m}, \ \forall m \in \mathfrak{M} \right\}.$$

For simplicity of notation and exposition in the rest of this section we assume that the traces $S \in \mathcal{S}$ are disjoint. This assumption can be removed at the cost of a more complex and heavy notation. Let us define for each trace $S \in \mathcal{S}$ a suitable space $\mathcal{U}^S$ and its dual that we denote by $\left(\mathcal{U}^S\right)'$. We define similar spaces on all the traces of fracture $F_i \ \forall i \in \mathfrak{I}$ and on the full set of traces $\mathcal{S}$:

$$\mathcal{U}^{\mathcal{S}_i} = \prod_{S \in \mathcal{S}_i} \mathcal{U}^S, \qquad \mathcal{U} = \prod_{i \in \mathfrak{I}} \mathcal{U}^{\mathcal{S}_i}.$$

For each trace S common to F_i and F_j we introduce suitable variables $U_i^S \in \mathcal{U}^S$ and $U_j^S \in \mathcal{U}^S$ representing the unknown quantities $[\frac{\partial H_i}{\partial \hat{\nu}_S^i}]_S$ and $[\frac{\partial H_j}{\partial \hat{\nu}_S^j}]_S$, respectively. Moreover, for each fracture F_i let us denote by

$$U_i = \prod_{S \in \mathcal{S}_i} U_i^S \in \mathcal{U}^{\mathcal{S}_i}$$

the tuple of functions U_i^S with $S \in \mathcal{S}_i$ and by $U = \prod_{i \in \mathfrak{I}} U_i \in \mathcal{U}$ the tuple of all functions U_i^S with $S \in \mathcal{S}_i$ and $i \in \mathfrak{I}$, i.e., the $2(\#\mathfrak{M})$-tuple of functions on all traces in $\bar{\Omega}$. Let us introduce the following linear bounded operators:

$$
\begin{aligned}
A_i &\in \mathcal{L}(V_i, V_i'), \quad \langle A_i H_i^0, v \rangle_{V_i', V_i} = \left(\mathbf{K}\,\nabla H_i^0, \nabla v\right), \ H_i^0 \in V_i, \\
A_i^D &\in \mathcal{L}(V_i^D, V_i'), \quad \langle A_i^D H_i^D, v \rangle_{V_i', V_i} = (\mathbf{K}\,\nabla H_i^D, \nabla v), \ H_i^D \in V_i^D, \\
B_i &\in \mathcal{L}(\mathcal{U}^{\mathcal{S}_i}, V_i'), \quad \langle B_i U_i, v \rangle_{V_i', V_i} = \langle U_i, v_{|_{\mathcal{S}_i}} \rangle_{\mathcal{U}^{\mathcal{S}_i}, \mathcal{U}^{\mathcal{S}_i\,'}}, \\
B_{\Gamma_{iN}} &\in \mathcal{L}(\mathrm{H}^{-\frac{1}{2}}(\Gamma_{iN}), V_i'), \quad \langle B_{\Gamma_{iN}} G_{iN}, v \rangle_{V_i', V_i} = \langle G_{iN}, v_{|_{\Gamma_{iN}}} \rangle_{\mathrm{H}^{-\frac{1}{2}}(\Gamma_{iN}), \mathrm{H}^{\frac{1}{2}}(\Gamma_{iN})}
\end{aligned}
$$

the definitions holding $\forall v \in V_i$. Further, we introduce the dual operators $A_i^* \in \mathcal{L}(V_i, V_i')$, $B_i^* \in \mathcal{L}(V_i, \mathcal{U}^{\mathcal{S}_i\,'})$ and the Riesz isomorphism $\Lambda_{\mathcal{U}^{\mathcal{S}_i}} : \mathcal{U}^{\mathcal{S}_i} \to \mathcal{U}^{\mathcal{S}_i\,'}$. Finally, let $\mathcal{R}_i\,H_{iD} \in V_i^D$ be a lifting of Dirichlet boundary condition H_{iD}. The problem is then clearly stated as follows: $\forall i \in \mathfrak{I}$ *find* $H_i = H_i^0 + \mathcal{R}_i\,H_{iD}$ *with* $H_i^0 \in V_i$ *such that*

$$(2.5) \qquad\qquad A_i H_i^0 = q_i + B_i U_i + B_{iN} G_{iN} - A_i^D\,\mathcal{R}_i\,H_{iD}.$$

2.1. Formulation as an optimization problem. The novel approach introduced in [6] consists in replacing the differential problems on the fractures (2.5) $\forall i \in \mathfrak{I}$, coupled with the matching conditions (2.2), (2.3), with a PDE constrained optimal control problem, in which the variable U acts as a control variable; equations (2.5) $\forall i \in \mathfrak{I}$ are the constraints, and the matching conditions are replaced by the task of minimizing a nonnegative functional. Let us define the spaces

$$\mathcal{H}^{\mathcal{S}_i} = \prod_{S \in \mathcal{S}_i} \mathcal{H}^S, \qquad \mathcal{H} = \prod_{i \in \mathfrak{I}} \mathcal{H}^{\mathcal{S}_i}$$

and the Riesz isomorphism $\Lambda_{\mathcal{H}^{\mathcal{S}_i}} : \mathcal{H}^{\mathcal{S}_i} \to \mathcal{H}^{\mathcal{S}_i\,'}$. We introduce the following linear bounded observation operators C_i^S and C_i and the dual C_i^*:

$$C_i^S \in \mathcal{L}(V_i, \mathcal{H}^S), \qquad C_i \in \mathcal{L}(V_i, \mathcal{H}^{\mathcal{S}_i}) = \prod_{S \in \mathcal{S}_i} C_i^S, \qquad C_i^* \in \mathcal{L}(\mathcal{H}^{\mathcal{S}_i\,'}, V_i').$$

For all $i \in \mathfrak{I}$, let us denote by $H_i(U_i)$ the solution to (2.5) corresponding to the value U_i for the control variable. Furthermore, for each fracture F_i, we denote by $\prod_{S \in \mathcal{S}_i} U_j^S$ the tuple of control functions defined on the fractures F_j intersecting F_i in the traces $S \in \mathcal{S}_i$.

Let us now introduce the following differentiable functional $J : \mathcal{U} \to \mathbb{R}$:

$$J(U) = \sum_{S \in \mathcal{S}} J^S(U) = \sum_{S \in \mathcal{S}} \left(||C_i^S H_i(U_i) - C_j^S H_j(U_j)||_{\mathcal{H}^S}^2 + ||U_i^S + U_j^S||_{\mathcal{U}^S}^2 \right)$$

$$(2.6) \qquad = \frac{1}{2} \sum_{i \in \mathfrak{I}} \left(|| \prod_{S \in \mathcal{S}_i} \left(C_i^S H_i(U_i) - C_j^S H_j(U_j) \right) ||_{\mathcal{H}^{S_i}}^2 + ||U_i + \prod_{S \in \mathcal{S}_i} U_j^S||_{\mathcal{U}^{S_i}}^2 \right).$$

The problem of finding the hydraulic head in the whole domain is restated as the following optimization problem: find $U \in \mathcal{U}$ solving the problem

$$(2.7) \qquad \min J(U) \quad \text{subject to (2.5)} \ \forall i \in \mathfrak{I}.$$

In [6] it is shown that if $\mathcal{U}^S = \mathrm{H}^{-\frac{1}{2}}(S)$ and $\mathcal{H}^S = \mathrm{H}^{\frac{1}{2}}(S)$, there exists a unique control variable U vanishing the functional $J(U)$ and correspondingly the unique solution H satisfying (2.5) $\forall i \in \mathfrak{I}$ is the solution to (2.1)–(2.3), as the vanishing of the two terms of the functional J corresponds to the imposition of the matching conditions (2.2), (2.3) $\forall m \in \mathfrak{M}$. It is further shown that the optimal control $U \in \mathcal{U}$ providing the minimum of the functional $J(U)$ is characterized by the following conditions:

$$(2.8) \qquad (\Lambda_{\mathcal{U}^{s_i}})^{-1} B_i^* P_i + U_i + \prod_{S \in \mathcal{S}_i} U_j^S = 0$$

$\forall i \in \mathfrak{I}$, where the functions $P_i \in V_i$ are the solution of

$$(2.9) \qquad A_i^* P_i = C_i^* \Lambda_{\mathcal{U}^{s_i}} \prod_{S \in \mathcal{S}_i} \left(C_i^S H_i(U_i) - C_j^S H_j(U_j) \right) \quad \text{in } F_i.$$

The computation of the solution to the problem of interest on the whole DFN may be approached by either solving problems (2.5) coupled with (2.8) and (2.9) $\forall i \in \mathfrak{I}$ or setting up an iterative process for solving the optimization problem (2.7). In the next section we will give details concerning computation of a numerical solution with these approaches.

Remark 2.1. The assumption of each trace being shared by exactly two fractures can be circumvented by redefining the functional as follows. With straightforward extension to more general cases, we allow three fractures F_i, F_j, F_k to share the same trace S. Then the corresponding $J^S(U)$ term in the definition of $J(U)$ is

$$J^S(U) = ||C_i^S H_i(U_i) - C_j^S H_j(U_j)||_{\mathcal{H}^S}^2 + ||C_i^S H_i(U_i) - C_k^S H_k(U_k)||_{\mathcal{H}^S}^2$$
$$+ ||U_i^S + U_j^S + U_k^S||_{\mathcal{U}^S}^2.$$

3. Discretization of the constrained optimization problem. In this section, we account for the numerical solution of the problem, and we start briefly sketching the derivation of the finite dimensional counterpart of problem (2.7). For simplicity, in this section we assume homogeneous Dirichlet boundary conditions, i.e., $H_D = 0$. All the results can be extended to the general case $H_D \neq 0$. We describe our numerical method for the approximation of the solution assuming $\mathcal{U}^S = \mathrm{L}^2(S)$, $\mathcal{H}^S = \mathrm{L}^2(S) \ \forall S \in \mathcal{S}$. We remark that with these choices the assumption of disconnected traces can be removed [6].

Let us introduce an independent conforming triangulation $\mathcal{T}_{\delta,i}$ on each fracture F_i $\forall i \in \mathfrak{I}$. Let $\mathrm{V}_{\delta,i}$ be the finite dimensional trial and test spaces defined on the elements of $\mathcal{T}_{\delta,i}$ and spanned by Lagrangian basis functions $\phi_{i,k}$, $k = 1,\ldots,N_i$. The discrete approximation of H_i on each fracture is defined as $h_i = \sum_{k=1}^{N_i} h_{i,k}\phi_{i,k} \ \forall i \in \mathfrak{I}$.

Let us consider the following different numbering for the control functions U_i^S, induced by the trace numbering. Let $S = S_m$ be a given trace with $I_{S_m} = \{i,j\}$ and assuming $i < j$, we denote by U_m^- and by U_m^+ the control functions related to the mth trace and corresponding to fractures F_i and F_j, respectively. Let us fix a finite dimensional subspace of $\mathcal{U}^S$ for the discrete approximation $u_m^\star$ of the control variable $U_m^\star$, $\star = -,+$ and let us introduce basis functions $\psi_{m,k}^-$, $k = 1,\ldots,N_m^-$ and $\psi_{m,k}^+$, $k = 1,\ldots,N_m^+$. Then we have for $m \in \mathfrak{M}$, $\star = -,+$, $u_m^\star = \sum_{k=1}^{N_m^\star} u_{m,k}^\star \psi_{m,k}^\star$.

With this notation, using L^2-norms in (2.6) and $C_i^S h_i = h_{i|_S}$, we obtain the following finite dimensional form of the functional $J(u)$:

$$J(u) = \frac{1}{2}\sum_{i\in\mathfrak{I}}\sum_{S\in\mathcal{S}_i}\int_S \left(\sum_{k=1}^{N_i} h_{i,k}\phi_{i,k|_S} - \sum_{k=1}^{N_j} h_{j,k}\phi_{j,k|_S}\right)^2 \,\mathrm{d}\gamma$$

$$(3.1)\qquad + \frac{1}{2}\sum_{m\in\mathfrak{M}}\int_S \left(\sum_{k=1}^{N_m^-} u_{m,k}^- \psi_{m,k}^- + \sum_{k=1}^{N_m^+} u_{m,k}^+ \psi_{m,k}^+\right)^2 \,\mathrm{d}\gamma.$$

In view of deriving a compact form for (3.1), let us introduce vectors $h_i \in \mathbb{R}^{N_i}$, $h_i = (h_{i,1},\ldots,h_{i,N_i})^T$, $i \in \mathfrak{I}$, and setting $N^F = \sum_{i\in\mathfrak{I}} N_i$, let $h \in \mathbb{R}^{N^F}$ be obtained concatenating, for $i \in \mathfrak{I}$, vectors h_i. Hence from now on, besides denoting the discrete solution, h_i will also denote the vector of degrees of freedom (DOFs). Similarly, let us introduce the vectors $u_m^\star \in \mathbb{R}^{N_m^\star}$, $u_m^\star = (u_{m,1}^\star,\ldots,u_{m,N_m^\star}^\star)^T$, $m \in \mathfrak{M}$, $\star = -,+$, and setting $N^T = \sum_{m\in\mathfrak{M}}(N_m^- + N_m^+)$ we define $u \in \mathbb{R}^{N^T}$ concatenating $u_1^-, u_1^+, \ldots, u_{\#\mathfrak{M}}^-, u_{\#\mathfrak{M}}^+$.

For all $i \in \mathfrak{I}$, $S \in \mathcal{S}_i$, let us define matrices $M_i^S \in \mathbb{R}^{N_i\times N_i}$ and (for $j \in J_i$) $M_{ij}^S \in \mathbb{R}^{N_i\times N_j}$ as

$$(M_i^S)_{k\ell} = \int_S \phi_{i,k|_S}\phi_{i,\ell|_S}\,\mathrm{d}\gamma, \qquad (M_{ij}^S)_{k\ell} = \int_S \phi_{i,k|_S}\phi_{j,\ell|_S}\,\mathrm{d}\gamma$$

and for $m \in \mathfrak{M}$ and $\star = -,+$ define $\mathcal{M}_m^\star \in \mathbb{R}^{N_m^\star\times N_m^\star}$, $\mathcal{M}_m^\pm \in \mathbb{R}^{N_m^-\times N_m^+}$, and $\mathcal{M}_m$ as

$$(\mathcal{M}_m^\star)_{k\ell} = \int_S \psi_{m,k}^\star \psi_{m,\ell}^\star\,\mathrm{d}\gamma, \quad (\mathcal{M}_m^\pm)_{k\ell} = \int_S \psi_{m,k}^- \psi_{m,\ell}^+\,\mathrm{d}\gamma, \quad \mathcal{M}_m = \begin{pmatrix} \mathcal{M}_m^- & \mathcal{M}_m^\pm \\ (\mathcal{M}_m^\pm)^T & \mathcal{M}_m^+ \end{pmatrix}.$$

Then, let $G^h \in \mathbb{R}^{N^F\times N^F}$ and $G^u \in \mathbb{R}^{N^T\times N^T}$ be defined blockwise as follows:

$$G_{ii}^h = \sum_{S\in\mathcal{S}_i} M_i^S, \ i\in\mathfrak{I}, \qquad G_{ij}^h = -M_{ij}^S, \ i\in\mathfrak{I}, \ j\in J_i, \qquad G^u = \mathrm{diag}(\mathcal{M}_1,\ldots,\mathcal{M}_{\#\mathfrak{M}}).$$

With these definitions at hand, the functional $J(u)$ in matrix form reads

$$J(u) = \frac{1}{2}h^T G^h h + \frac{1}{2}u^T G^u u.$$

Matrices G^h and G^u are clearly symmetric and semidefinite.

Now, let us turn our attention to the algebraic counterparts of operators A_i, B_i in (2.5): overloading notation, we let A_i and B_i also denote the matrices defining the algebraic operators. We set $A_i \in \mathbb{R}^{N_i\times N_i}$ and $B_i^{S_m} \in \mathbb{R}^{N_i\times N_m^\star}$ as

$$(3.2) \qquad (A_i)_{k\ell} = \int_{F_i} \nabla\phi_{i,\ell} \nabla\phi_{i,k} \ dF_i, \quad \left(B_i^{S_m}\right)_{k\ell} = \int_{S_m} \phi_{i,k\,|_{S_m}} \psi_{m,\ell}^\star \, \mathrm{d}\gamma,$$

where, since $S_m \subseteq \bar{F}_i \cap \bar{F}_j$, we take $\star = -$ if $i < j$ or $\star = +$ otherwise. Matrices $B_i^{S_m}$, $S_m \in \mathcal{S}_i$, are then grouped rowwise to form the matrix $B_i \in \mathbb{R}^{N_i \times N_{\mathcal{S}_i}}$ with $N_{\mathcal{S}_i} = \sum_{S_m \in \mathcal{S}_i} N_m^\star$ and $\star$ chosen as before, which acts on a column vector u_i obtained appending the blocks $u_m^\star$ in the same order used for $B_i^{S_m}$, as the action of a suitable operator $R_i : \mathbb{R}^{N^T} \mapsto \mathbb{R}^{N_{\mathcal{S}_i}}$ such that $u_i = R_i u$. According to these definitions, the constraints (2.5) lead to the algebraic equations

$$(3.3) \qquad\qquad A_i h_i - B_i R_i u = \tilde{q}_i, \qquad i \in \mathfrak{I},$$

where $\tilde{q}_i$ accounts for the term q_i in (2.5) and the boundary conditions. Denoting $w = (h^T, u^T)^T \in \mathbb{R}^{N^F + N^T}$ and defining

$$A = \mathrm{diag}(A_1, \ldots, A_{\#\mathfrak{I}}) \in \mathbb{R}^{N^F \times N^F}, \qquad B = \begin{pmatrix} B_1 R_1 \\ \vdots \\ B_{\#\mathfrak{I}} R_{\#\mathfrak{I}} \end{pmatrix} \in \mathbb{R}^{N^F \times N^T},$$

$$(3.4) \qquad C = (A \quad -B) \in \mathbb{R}^{N^F \times N^F + N^T}, \qquad G = \mathrm{diag}(G^h, \ G^u),$$

the overall problem reads as the following equality constrained quadratic programming problem:

$$(3.5) \qquad\qquad \min_w \frac{1}{2} w^T G w \qquad \text{s.t. } C w = \tilde{q}.$$

Classical results (see, e.g., [22, Theorem 16.2]) show that under proper assumptions on C and G, w^* is the unique global solution to (3.5) if and only if it is the unique solution to the following saddle point system:

$$(3.6) \qquad\qquad \mathcal{A} = \begin{pmatrix} G & C^T \\ C & 0 \end{pmatrix}, \qquad \mathcal{A} \begin{pmatrix} w^* \\ -p^* \end{pmatrix} = \begin{pmatrix} 0 \\ \tilde{q} \end{pmatrix},$$

where p^* is the vector of Lagrange multipliers. In [6] the following result, concerning existence and uniqueness of the solution to the discrete counterpart of problem (2.7), is proved.

THEOREM 3.1. *Let us consider the discrete formulation* (3.5) *to the problem of subsurface flow in a DFN with G and C defined as in* (3.4). *Then, the solution exists and is unique and coincides with the solution to* (3.6).

The numerical approximation of the hydraulic head can be obtained in a twofold manner. A possible method consists in solving the saddle point linear system (3.6). This approach is viable for DFNs of moderate size: in this case sparse solvers can efficiently compute a solution to (3.6). When very large DFN systems come into play, solving the linear system may be a quite demanding task even if very coarse meshes are used on each fracture, and parallel computing may become preferable. In these cases, as depicted in [6], a worthwhile approach consists in using a gradient-based method for the minimization of (3.5). Indeed, as shown in [6], this method allows for the decoupled solution of local problems on the fractures with a moderate exchange of information among them. This point makes the method appealing for parallelization on massively parallel computers and GPU-based computers, in which the local problems on fractures can be distributed among processors.

4. XFEM discretization.

4.1. XFEM description. The XFEM [3, 20, 11, 4] is a finite-element-based numerical method to approach partial differential equations in variational form with nonsmooth or discontinuous solutions. XFEM in the context of poro-fractured media are also used in [10]. The nonsmooth behavior of the solution is added to the standard finite element approximation space through customized enrichment functions in order to extend approximation capabilities. By means of the partition of unity method [1], the influence of the enrichments is localized in a neighborhood of irregularity interfaces. In this way the XFEM allows us to reproduce irregularities regardless of the underlying triangulation.

Let us consider a problem set on a domain $\omega \subset \mathbb{R}^d$ with a weak discontinuity (i.e., a discontinuity in derivatives) along the manifold $S \subset \omega, S \subset \mathbb{R}^{d-1}$, and let $\mathcal{T}_\delta$ be a conforming triangulation on ω with N^{el} elements $\tau_e \subset \mathbb{R}^d$, $\bar{\omega} = \bigcup_{1 \leq e \leq N^{el}} \tau_e$. Let V_δ^{fem} be the standard finite dimensional trial and test space defined on the elements of $\mathcal{T}_\delta$ and spanned by Lagrangian basis functions ϕ_k, $k \in \mathcal{I}$. Each basis function ϕ_k has compact support denoted by Δ_k.

If the nonsmooth character of the solution is a priori known, it is possible to introduce it in the FEM discrete space. Let us assume Φ is a continuous bounded function on ω, $\Phi \in H^1(\omega) \cap C^0(\bar{\omega})$ that well approximates the behavior of a function h in a neighborhood Δ_S of S given by the union of some mesh elements τ_e. It is possible to build a partition of unity on Δ_S based on the standard finite element shape functions to define new *enriching* basis functions starting from Φ that can be introduced into the FEM space, thus giving the enriched functional space

$$(4.1) \qquad V_\delta^{xfem} = \mathrm{span} \left(\{\phi_k\}_{k \in \mathcal{I}}, \{\phi_k \Phi\}_{k \in \mathcal{J}} \right),$$

where $\mathcal{J} \subset \mathcal{I}$ is the subset of indices of functions ϕ_k used to define the partition of Δ_S. DOFs in $\mathcal{J}$ are called enriched DOFs (and the corresponding nodes enriched nodes). The selection of the domain Δ_S can vary with the specific application of the method but is usually given by the union of mesh elements intersected by the interface S. The approximate solution h^{xfem} of the problem with the XFEM will be in general

$$(4.2) \qquad h_\delta^{xfem}(\hat{x}) = \sum_{k \in \mathcal{I}} h_k^{xfem} \phi_k(\hat{x}) + \sum_{k \in \mathcal{J}} a_k^{xfem} \phi_k(\hat{x}) \Phi(\hat{x}),$$

where h_k^{xfem} and a_k^{xfem} are the unknowns related to the standard and enriching basis functions, respectively. The nonsmoothness of the exact solution is now present in the discrete solution and is reproduced independently of the position of mesh elements. Since only a subset of total DOFs is enriched, elements in $\mathcal{T}_\delta$ may have a variable number of enriched nodes. In particular, according to the classification given in [16] we have *standard* elements when no nodes are enriched, *reproducing* elements if all nodes are enriched, and *blending* elements if only some nodes are enriched.

The enrichment function Φ can be correctly reproduced only in reproducing elements where the partition of unity is complete. On the contrary, in the blending elements partition of unity is partially established and unwanted terms are introduced in the approximation, affecting the convergence rate of the standard finite element [9, 29, 17]. Moreover, the basis of V_δ^{xfem} is no longer a Lagrangian basis. For these reasons we will actually implement the modified version of XFEM with shifted basis functions, as suggested in [17]. The enrichment basis function $\phi_k \Phi$ is replaced by

$$\phi_k(\hat{x})\widetilde{\Phi}(\hat{x}) = \phi_k(\hat{x})R(\hat{x})\left(\Phi(\hat{x}) - \Phi(\hat{x}_k)\right),$$
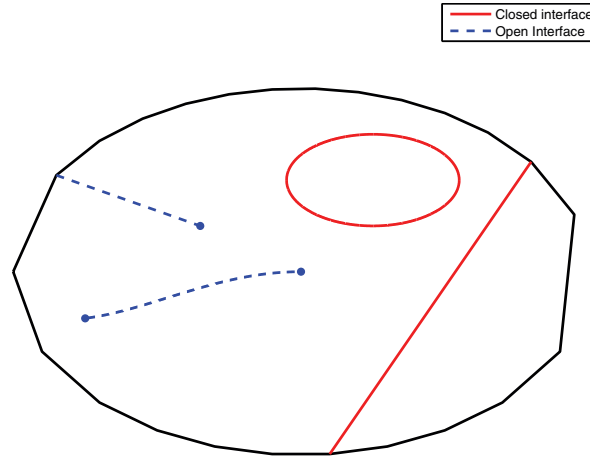
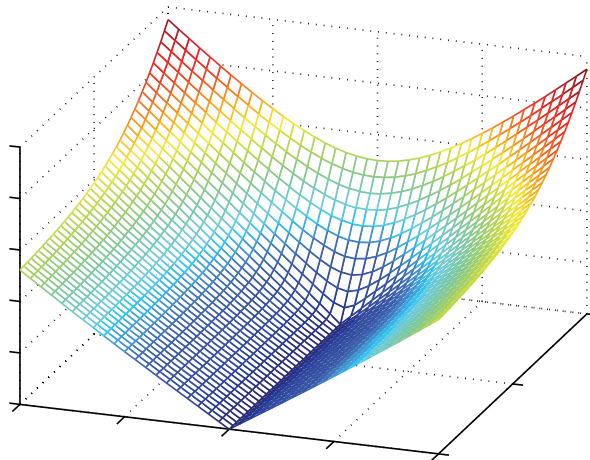FIG. 4.1. *Classification of discontinuity interfaces.*

FIG. 4.2. *Example of function behaviour for near-tip enrichments.*

where $R(\hat{x}) = \sum_{j \in \mathcal{J}} \phi_j(\hat{x})$ and $\hat{x}_k$ are the coordinates of the kth node. The enriched domain is extended including blending elements through a redefinition of the set $\mathcal{J}$ as $\widetilde{\mathcal{J}} = \{k \in \mathcal{I} : \Delta_k \cap \mathring{\Delta}_\Phi \neq \emptyset\}$, where $\Delta_\Phi = \bigcup_{k \in \mathcal{J}} \Delta_k$. In this way the approximation capability of the enriched space is unaffected in reproducing elements, where $R(\hat{x}) = 1$, and depends on the choice of the enrichment function Φ, while the standard finite element polynomial representation of solution can now be obtained in blending elements, restoring optimal convergence rates. The shift restores Lagrangian property of the basis functions, making easier the imposition of Dirichlet boundary conditions and graphical representation of the results.

The generalization to multiple enrichments is straightforward. In particular we remark that XFEM enjoys an additivity property with respect to the interfaces: independently of traces disposition, the set of enriching functions with multiple interfaces is the union of the enrichments introduced by each interface. A comprehensive review of the XFEM method, including implementation details, can be found in [16].

4.2. Enrichment functions selection. We now focus on the definition of the enrichments used in the application of the XFEM to DFNs. Recalling definitions introduced in section 2, on each fracture F_i the exact solutions H_i to (2.5) may have a jump of fluxes across the traces in $\mathcal{S}_i$. The XFEM approach allows the triangulation to be set on each fracture independently of the disposition and number of the traces, thus actually eliminating meshing problems related to DFNs. Let us fix a fracture $F \subset \mathbb{R}^2$ and let $\mathfrak{M}_F \subset \mathfrak{M}$ be the subset of indices corresponding to traces on F.

The selection of the enrichment functions is related to the irregularity to be reproduced and to the type of interfaces. Here we deal with solutions with discontinuous gradient (*weak* discontinuities) and different enrichment functions need to be employed according to the location of the traces (interfaces) in the domain, with a distinction between *closed* and *open* interfaces (see Figure 4.1). In order to describe the enrichment functions, let us introduce for $m \in \mathfrak{M}_F$ the function $d_m(\mathbf{x})$ given by the signed distance from S_m [29, 4]: for $\hat{x} \in F$, $d_m(\hat{x}) = \|\bar{x} - \hat{x}\|\operatorname{sign}(\hat{n}_{S_m} \cdot (\bar{x} - \hat{x}))$, where $\bar{x}$ is the projection of $\hat{x}$ on S_m and $\hat{n}_{S_m}$ is the fixed unit normal vector to S_m.

For a *closed* interface we use the enrichment function Ψ^m defined as $\Psi^m(\hat{x}) = |d_m(\hat{x})|$ [4] that is a continuous function with discontinuous first order derivatives across S_m. This introduces the required nonsmooth behavior in the approximation. The enrichment is localized in a neighbourhood of S_m defined by the set of DOF $\mathcal{J}_\Psi^m = \{k \in \mathcal{I} : \Delta_k \cap S_m \neq \emptyset\}$.

On the contrary, if S_m is an *open* interface, different enrichment functions are needed to reproduce the behavior of the solution close to the extrema of the interface and away from the extrema $\{s^1, s^2\} = \sigma_m$. Away from the extrema, the nonsmooth behavior of the solution is similar to the case of closed interfaces and the same function Ψ^m is used, being the set $\mathcal{J}_\Psi^m$ defined as $\{k \in \mathcal{I} : \Delta_k \cap S_m \neq \emptyset, \Delta_k \cap s^\ell = \emptyset\}$ $\forall s^\ell \in \sigma_m$. Other enrichment functions are introduced to describe near-tip behavior of the solution; we adopt here the functions suggested in [4] and defined as follows. Let r be the signed distance between the current point and trace tip; furthermore, let us consider for each tip a reference system centered into trace tip with the x-axis aligned to the trace and oriented in such a way that the trace lies on the negative side, and let $\theta \in (-\pi, \pi)$ be the polar angle of $\hat{x}$ in this system. Then, the enriching functions are

$$\Theta_{s^\ell}^m(\hat{x}) \in \left\{ r \cos \frac{\theta}{2}, r^2 \cos \frac{\theta}{2}, \sqrt{r} \cos \frac{\theta}{2} \right\}, \qquad s^\ell \in \sigma_m.$$

Functions $\Theta_{s^\ell j}^m(\hat{x})$ are continuous and cusplike on S_m, and their behavior around trace tips is a combination of $\{\sqrt{r}, r, r^2\}$, as shown in Figure 4.2, in which we plot the function $r \cos \theta/2$. The set of DOFs subject to tip enrichments is given by $\mathcal{J}_{\Theta s^\ell}^m = \{k \in \mathcal{I} : \Delta_k \cap s^\ell \neq \emptyset\}$ $\forall s^\ell \in \sigma_m$. In order to prevent blending elements related problems, the enrichment functions described here are used as a basis for the modified XFEM version [17] mentioned in the previous subsection.

With all the enrichments described here, the number of DOFs on each fracture F_i is $N_i = \#\mathcal{I} + \sum_{m \in \mathfrak{M}} \#\widetilde{\mathcal{J}}^m + 3 \sum_{m \in \mathfrak{M}} \sum_{s^\ell \in \sigma_m} \#\widetilde{\mathcal{J}}_{\Theta s^\ell}^m$, where $\widetilde{\mathcal{J}}^m$ and $\widetilde{\mathcal{J}}_{\Theta s^\ell}^m$ denote the sets of DOFs for the modified version.

The numerical integration of singular functions was performed on subdomains not crossing the traces [20, 4]. A Gauss quadrature rule was used with special care for the integration of gradients of near-tip enrichment functions, where a concentration of integration nodes around trace tip is recommended to correctly evaluate the singularities [19].

5. Numerical results. The numerical simulations reported in this section aim at showing the viability of the approach proposed in [6] in solving problems on complex networks. In subsection 5.1 a problem with open interfaces is considered, and numerical convergence of the method is analyzed. In subsection 5.2 a critical situation is introduced in which three traces are very close to each other and almost parallel and intersecting each other. The great deal of flexibility in mesh generation allowed by our approach is shown. In subsection 5.3 some more complex DFNs are considered. In subsection 5.4 preconditioning issues for system (3.6) are analyzed. Finally, in 5.5 we show how the method can deal with broadly ranging transmissivity values.

All the simulations are performed with triangular meshes and first order finite elements. The problems have been solved through the optimization approach introduced in [6], in conjunction with extended finite elements, and mesh elements arbitrarily placed with respect to the traces. We highlight that since the triangulations on a couple of intersecting fractures induce different discretizations on the common trace, the minimum of the discrete functional (3.1) is different from zero, which is the theoretical minimum of the functional in the continuous case.

The problems have been solved in a twofold manner: either solving the whole system (3.6) via an iterative method or applying the steepest descent method to problem (3.5) (Algorithm 4.5 in [6]). Concerning the first case, the matrix $\mathcal{A}$ in (3.6) is symmetric but indefinite, as shown in classic literature on saddle point problems (see, e.g., [5]). Furthermore, in real applications $\mathcal{A}$ is of huge dimensions but highly sparse, hence an iterative method with matrix free approach appears to be a suitable choice. Among iterative methods for solving linear systems, SYMMLQ [24] is recommended for symmetric indefinite systems and requires a symmetric positive definite preconditioner. This is the choice we adopted here, using the MATLAB built-in SYMMLQ function. The issue of preconditioning SYMMLQ on DFN applications is addressed in subsection 5.4.

Nevertheless, when large DFNs are considered, even assembling and storing the system (3.6) may be a quite demanding task. The steepest descent method suggested in [6] may help in this respect as only the decoupled solution of local problems on fractures are required at each step, and with this approach a large problem can be dealt with also on a simple PC without requiring excessive memory resources. When this algorithm is used, the local problems (3.3) are typically of small dimension, so that a direct solver can be effectively used to compute these solutions. We used in our experiments the MATLAB built-in direct solver. Computations are always started from $u^0 = 0$.

5.1. Behavior of the method with open interfaces. The first problem proposed is designed in order to test the behavior of the method with near-tip enrichments. Let us define the domain $\Omega = F_1 \cup F_2$ with

$$F_1 = \left\{ (x, y, z) \in \mathbb{R}^3 : -1 < x < 1, \ -1 < y < 1, \ z = 0 \right\},$$
$$F_2 = \left\{ (x, y, z) \in \mathbb{R}^3 : -1 < x < 0, \ y = 0, \ -1 < z < 1 \right\}.$$

The trace S ends in the interior of F_1 and is an open interface. Let us define $H^{ex}(x, y, z)$ in Ω as

$$H^{ex}(x, y, z) = \left\{ \begin{array}{ll} (x^2 - 1)(y^2 - 1)(x^2 + y^2) \cos\left(\frac{1}{2} \arctan2(x, y)\right) & \text{on } F_1, \\ -(z^2 - 1)(x^2 - 1)(z^2 + x^2) \cos\left(\frac{1}{2} \arctan2(z, x)\right) & \text{on } F_2, \end{array} \right.$$

where $\arctan2(x, y)$ is the four-quadrant inverse tangent, giving the angle between the positive x-axis and point (x, y), and differs from the usual one-argument inverse

tangent $\arctan(\cdot)$ for placing the angle in the correct quadrant. The function H is the solution of the system

$$
\begin{aligned}
-\Delta H &= -\Delta H^{ex} && \text{in } \Omega \setminus \mathrm{S}, \\
H &= 0 && \text{on } \partial F_1 \cup \partial F_2 \setminus \Gamma, \\
H &= \frac{\sqrt{2}}{2}(z^2 - z^4) && \text{on } \Gamma,
\end{aligned}
$$

where Γ is the boundary of F_2 parallel to the z-axis and intersecting the x-axis in $x = -1$. In Figure 5.1, left, we report the geometry of the problem and the nonconforming mesh used with XFEM ($\delta_{\max} = 0.1$). On the right, we report the control variable u_1 computed, compared with the exact function. The flux mismatch computed along the trace is $\|u_1 + u_2\|_{\mathrm{L}^2(S)} = 2.8\,10^{-4}$. The results obtained with XFEM are shown in Figure 5.2. The problem has also been solved with standard finite elements on meshes conforming to the trace. The rates of convergence in both cases, reported in Figure 5.3, left, are optimal. As expected, the curves relative to the solution obtained with the XFEM lie below the curves corresponding to standard finite elements. In fact, the basis function $r^2 \cos\theta/2$ introduced for trace tip behaves essentially as H^{ex} close to the center of F_1, where tip is located, thus locally reducing the error with respect to the standard finite elements. Minima of $\sqrt{J}$ are reported on the right plot of Figure 5.3, showing that grid refinement pushes these minima toward zero.

5.2. Critical traces disposition and DOFs investigation. In this subsection we consider a problem with critical traces disposition. We consider four fractures: F_1 is located on the $x - y$ plane of a 3D reference system; the other three fractures are orthogonal to the $x - y$ plane and generate with F_1 three traces very close to each other and almost parallel, i.e., the angles between traces are very small, ranging from 0.8 (sexagesimal) degrees up to 1.8 degrees. The three traces are open interfaces. The fracture F_1 and the three traces are represented in Figure 5.4, along with examples of mesh used on F_1. On the right plot, a detail of the right extremities of the traces is shown. The coordinates of traces extremities are $(x_1^b, y_1^b) = (0.4, 0.5)$, $(x_1^e, y_1^e) = (0.6, 0.5)$, $(x_2^b, y_2^b) = (0.398, 0.5)$, $(x_2^e, y_2^e) = (0.602, 0.503)$, $(x_3^b, y_3^b) = (0.402, 0.501)$, $(x_3^e, y_3^e) = (0.598, 0.498)$.

In Table 5.1 we report, for fracture F_1, the number of DOFs obtained meshing the fracture for the following approaches: our optimization approach in conjunction with
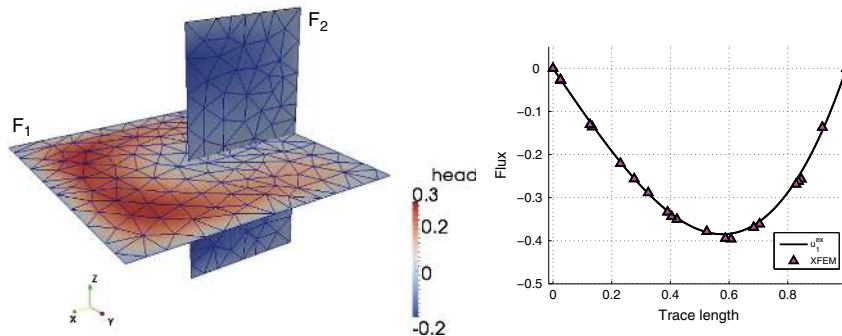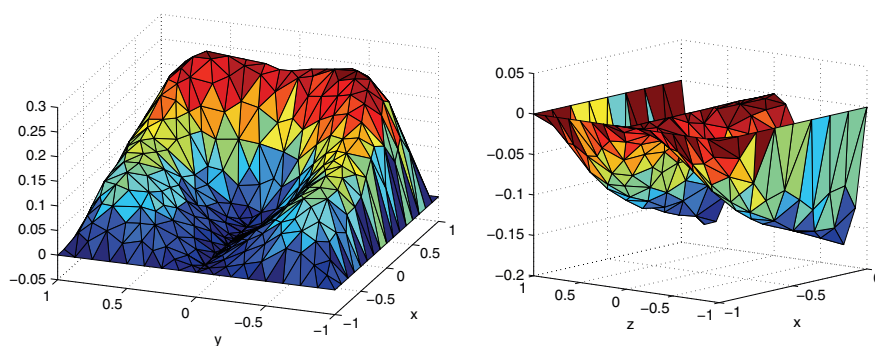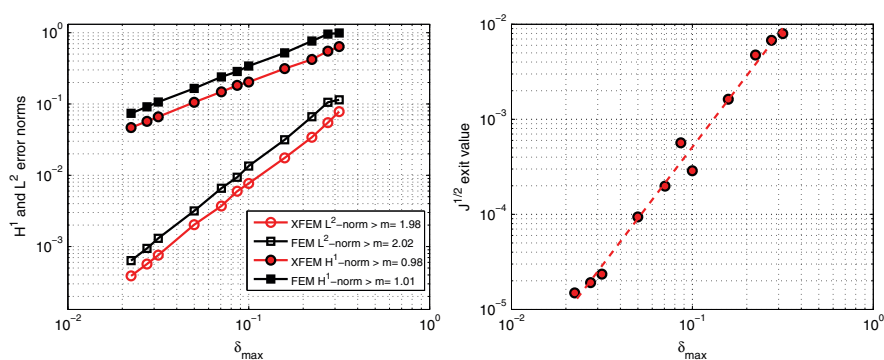

FIG. 5.1. *Problem 1: Domain description with mesh and solution h (left) and control variable along trace (right).*

FIG. 5.2. *Problem 1: Numerical solution on F_1 (left) and on F_2 (right).*

FIG. 5.3. *Problem 1: $\mathrm{H}^1(\Omega)$ and $L^2(\Omega)$ error norms (left) and functional minima (right) under refinement.*

TABLE 5.1
Number of DOFs for fracture F_1 for different solution strategies.

$A_{\max}$	XFEM	Nonfitting FEM	Fitting FEM
0.05	48	12	655
0.0225	85	34	672
0.01	135	71	715
0.0025	398	311	910
0.0004	486	396	1017

XFEM, hence without fitting the mesh to the traces; the same optimization approach, on the same mesh, with standard FEM basis functions (hence without enriching basis functions); and standard FEM on a mesh fitting the traces. We remark that in this latter case the mesh has been generated only on F_1 and is only constrained to fit trace disposition; if the mesh on the other three fractures were generated, and conformity on all the DFN were required, the number of DOFs might be even larger. In all three cases the meshes have been obtained with the software `Triangle` [28], requiring a good quality mesh ($-q$ option in `Triangle`) and imposing a given maximum element area $A_{\max}$, reported in Table 5.1. Comparing the first and second columns of the table, it is clear that when the same mesh is considered, XFEM requires a larger number of DOFs than FEM, with a more significant percentage on the coarser meshes, since a larger fraction of elements are subject to enrichment. Under grid refinement, the number of elements enriched increases, but the percentage decreases, and the relative

difference in DOFs between the two approaches becomes smaller. As shown by the last column, the number of DOFs introduced with a regular, fitting mesh is in this case much higher than the previous ones, thus showing how effective our approach is in reducing the number of DOFs with respect to a conforming approach. Besides, we stress that nonfitting meshes are produced without any knowledge about traces disposition and thus are easily obtained.

A problem has been introduced on this DFN as follows: $-\Delta H = 0$ in $\Omega\backslash S$; on F_1 we set homogeneous Dirichlet conditions on fracture edges (almost) parallel to the traces and homogeneous Neumann condition on the other sides; on fractures F_i, $i = 2, 3, 4$, we set $H = 1$ on the top edge and homogeneous Neumann conditions on the other sides. The problem has been solved with the first two approaches mentioned earlier (XFEM and FEM on the same mesh, with our optimization approach). A coarse ($A_{\max} = 0.05$) and a fine ($A_{\max} = 0.0025$) mesh have been used and are depicted in Figure 5.4. The numerical results obtained on the coarse and fine meshes are reported in Figures 5.5 and 5.6, respectively. The XFEM solutions are plotted on subelements generated by cutting XFEM elements along traces. Finally, in Figure 5.7 we report the values of $\sqrt{J}$ versus the number of iterations of the steepest descent method using both FEM and XFEM on the coarse mesh. It can be seen that the larger number of DOFs introduced by enrichments, and the larger number of iterations required by XFEM, are counterbalanced by the higher quality of the solution.
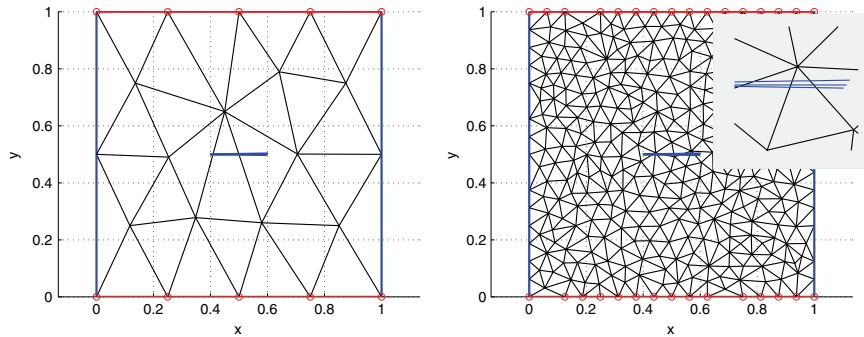
FIG. 5.4. *Problem 2: meshes on F_1. Left: coarse grid; right: fine grid.*
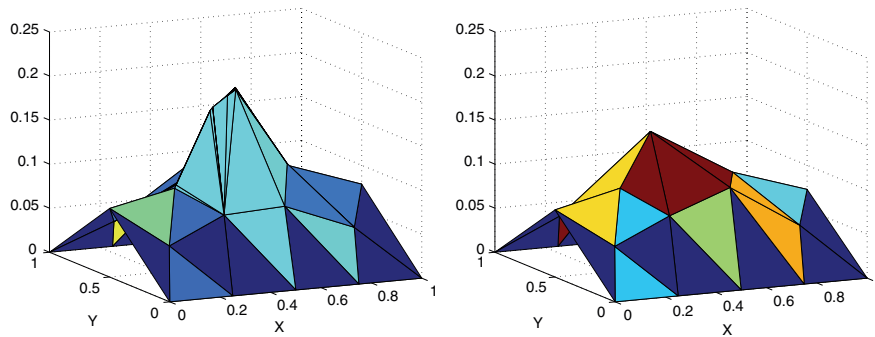
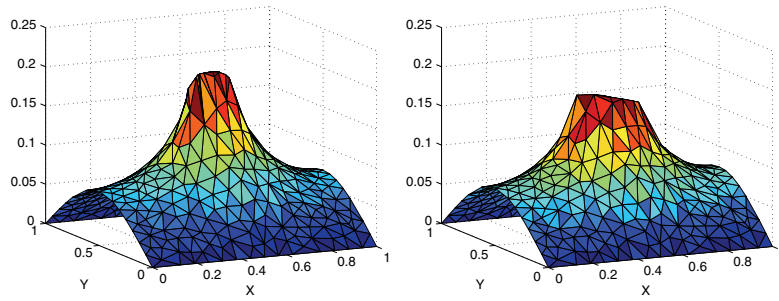FIG. 5.5. *Problem 2: Solution on coarse grid. Left: XFEM; right: FEM.*

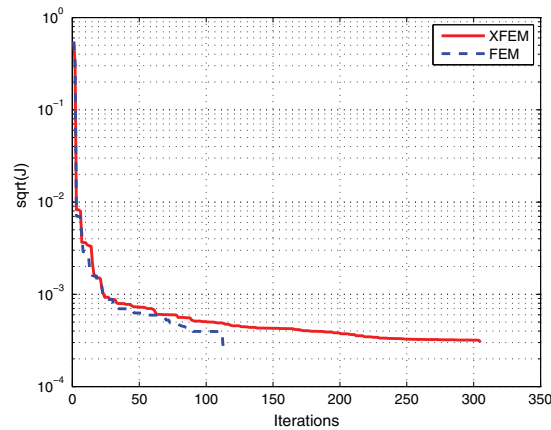FIG. 5.6. *Problem 2: Solution on fine grid. Left: XFEM; right: FEM.*

FIG. 5.7. *Problem 2: values of $\sqrt{J}$ against number of iterations.*

5.3. DFN systems simulations. In this subsection we consider systems of fractures of increasing complexity. Fracture transmissivities K_i are assumed constant on each fracture but different from fracture to fracture.

First, we consider the DFN configuration depicted in Figure 5.8: the system is composed of six fractures. Some of the traces generated do intersect each other. A
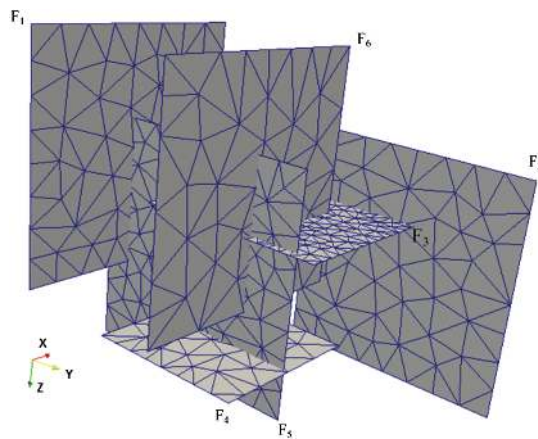
FIG. 5.8. *Problem 6F: Geometry with a coarse mesh.*
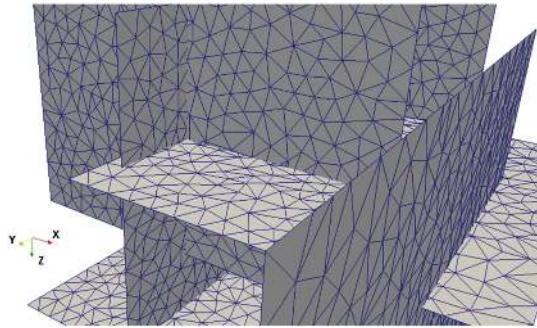
FIG. 5.9. *Problem 6F: detail of fine mesh.*
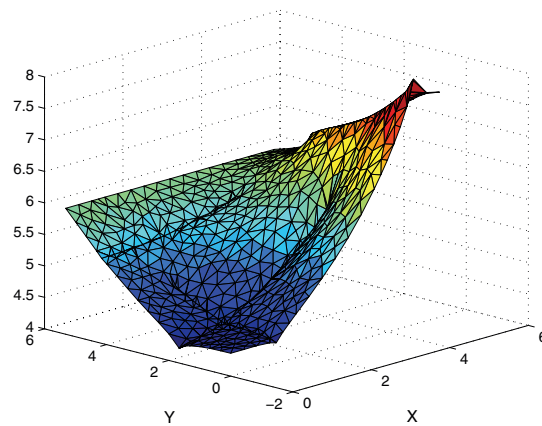
FIG. 5.10. *Problem 6F: solution on F_2 with fine mesh.*

detail of the mesh, presented in Figure 5.9, highlights nonconformity of the mesh. The numerical solution computed on fracture F_2 is reported in Figure 5.10, and is represented with respect to a local tangential reference system (X, Y). This convention also applies from now on to similar plots of the solutions. The figure shows that intersecting traces are easily handled by our approach. In particular, we see in Figure 5.10 that the discontinuities in the flux along the traces are clearly shown. In Figure 5.11 we report the solution computed on fracture F_6 with a coarse and a fine
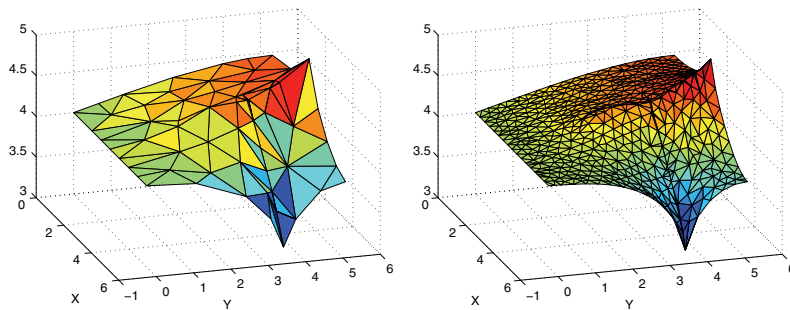
FIG. 5.11. *Problem 6F: solution on F_6 with coarse (left) and fine (right) mesh.*

Copyright © by SIAM. Unauthorized reproduction of this article is prohibited.
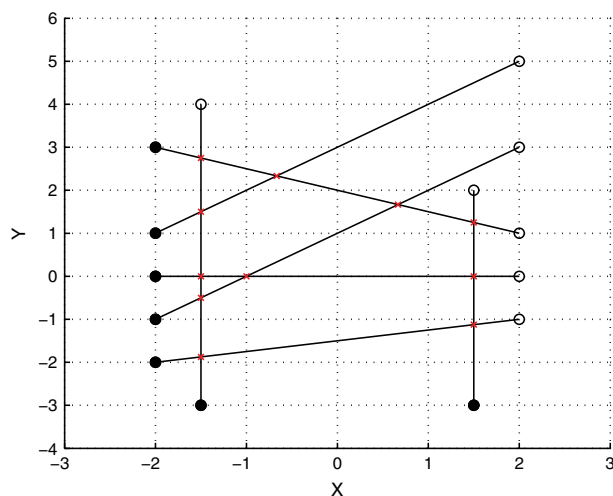
FIG. 5.12. *Problem* 7F: *Domain description.*

mesh ($\delta_{\max} = 0.77$ and $\delta_{\max} = 0.22$, respectively), showing the behavior of the solution close to intersecting traces. The solutions are plotted on subelements obtained splitting XFEM elements along traces.

Then, the following configurations are considered. In these problems the reference system for $\mathbb{R}^3$ is a right-handed orthogonal system oriented such that the $x - y$ plane lies on the page plane and fractures are parallel to z axis.

- 7F: The domain is composed of 7 fractures and 11 traces, as shown in Figure 5.12. Fractures range from $z = 0$ to $z = 5$. All the traces completely cross each fracture, and thus tip enrichments are not used.
- 11F: The domain is composed of 11 fractures and 26 traces, as shown in Figure 5.13. The fracture shown by a dashed line ranges from $z = 0$ to $z = 2.5$, while all other fractures range from $z = 0$ to $z = 5$; thus in this case tip enrichment functions are employed, since some traces end inside the domain.
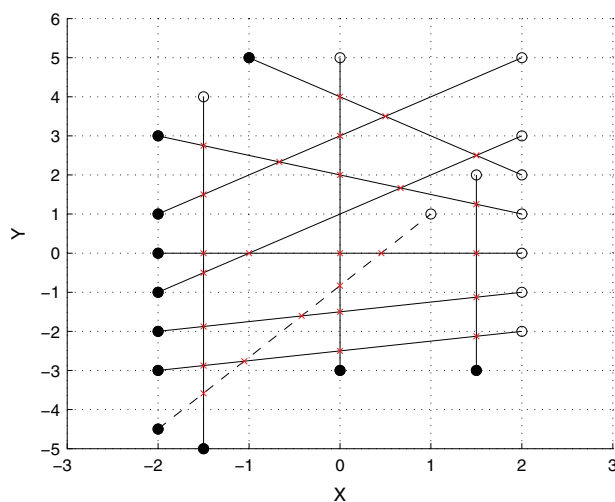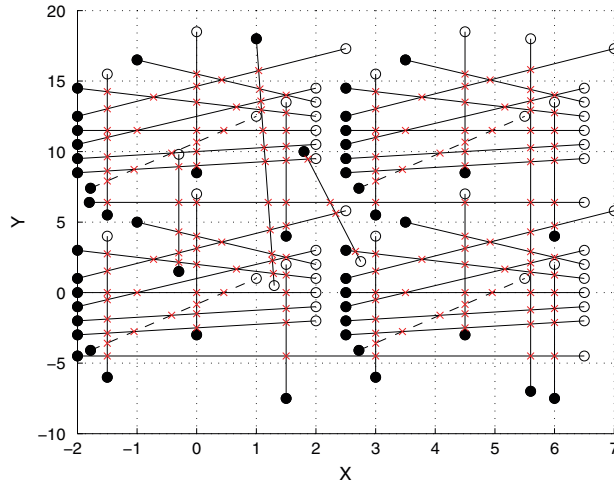

FIG. 5.13. *Problem* 11F: *Domain description.*

FIG. 5.14. *Problem* 50*F: Domain description.*

50F: In this last case the domain is composed of 50 fractures and 153 traces, as sketched in Figure 5.14. All fractures in continuous lines range between $z = 0$ and $z = 3$, while fractures drawn with dashed lines range from $z = 0$ to $z = 1.5$. Also in this case tip enrichment functions are employed.

Boundary conditions are set in a similar fashion in all cases. Homogeneous Dirichlet boundary conditions are set on $\Gamma_D = \partial\Omega \cap \{z = 0\}$, while $\Gamma_N = \partial\Omega \setminus \Gamma_D$. A different constant value of Neumann boundary condition is imposed on fracture edges belonging to Γ_N and marked with a plain black dot in the figures showing domain configurations. Homogeneous Neumann boundary conditions are placed on the other fracture edges in Γ_N. In all cases different (constant) values of K are randomly taken on each fracture, approximately ranging from 10^{-1} to 10^2. The geometry of the DFN and a mesh example are reported in Figure 5.15 for the case 11F. In Figures 5.16–5.21 and 5.23–5.25 we report for each system considered and for a selected fracture F_i: (i) the solution h_i on the fracture; (ii) the restriction on the traces of h_i and of the solution h_j obtained on the fracture F_j which generates the trace through its intersection with F_i; (iii) the control variables u_i and $-u_j$. All the results
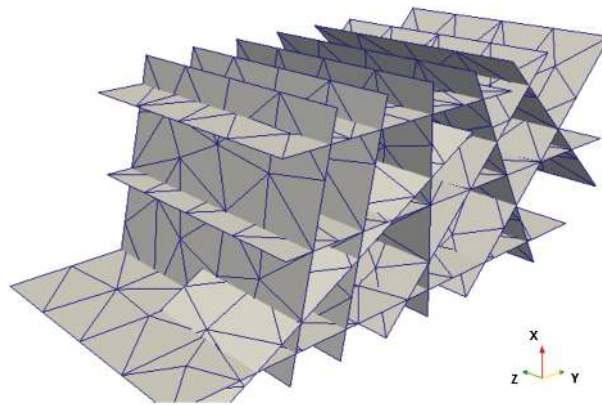
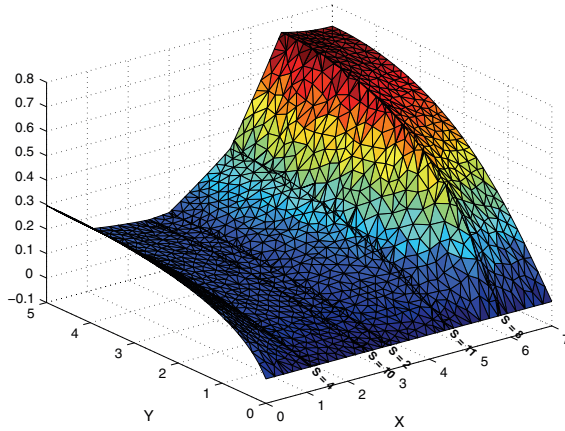FIG. 5.15. *Problem* 11*F: geometry and a viable coarse mesh* ($\delta_{\max} = 1$).

FIG. 5.16. *Problem 7F: Solution on fracture F_6 (traces numbering is global).*
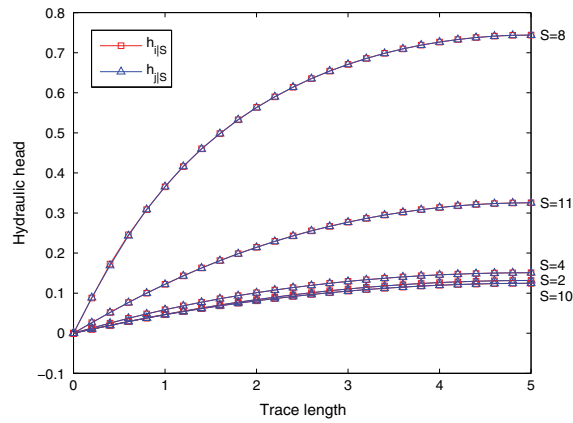

FIG. 5.17. *Problem 7F: Solution h_i on the traces of fracture F_6 and solutions $\{h_j\}$ on the fractures intersecting F_6 in its traces.*
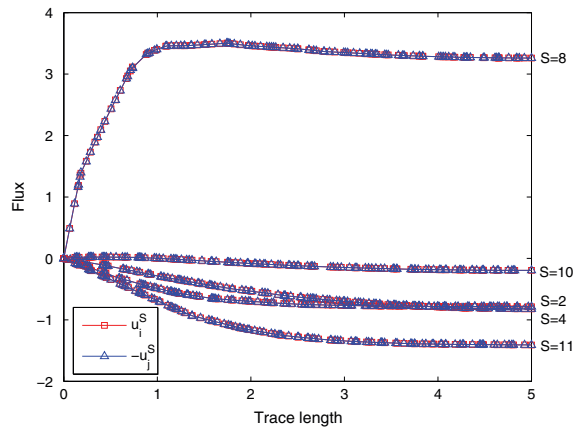

FIG. 5.18. *Problem 7F: Solution u_i on the traces of fracture F_6 and solutions $\{-u_j\}$ on the fractures intersecting F_6 in its traces.*
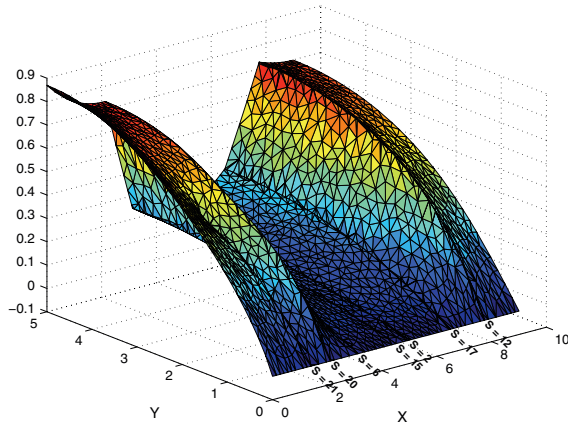
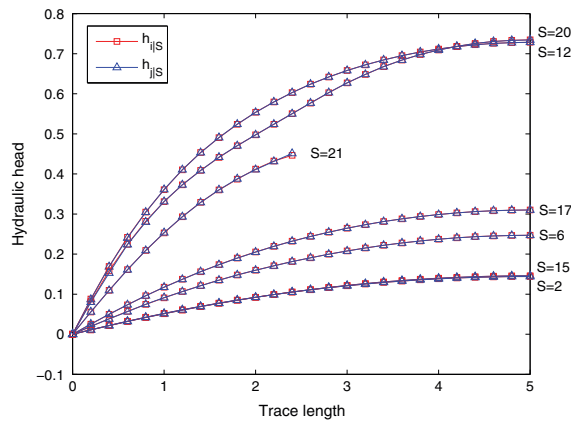FIG. 5.19. *Problem* 11F: *Solution on fracture* F_6 *(traces numbering is global).*

FIG. 5.20. *Problem* 11F: *Solution* h_i *on the traces of fracture* F_6 *and solutions* $\{h_j\}$ *on the fractures intersecting* F_6 *in its traces.*
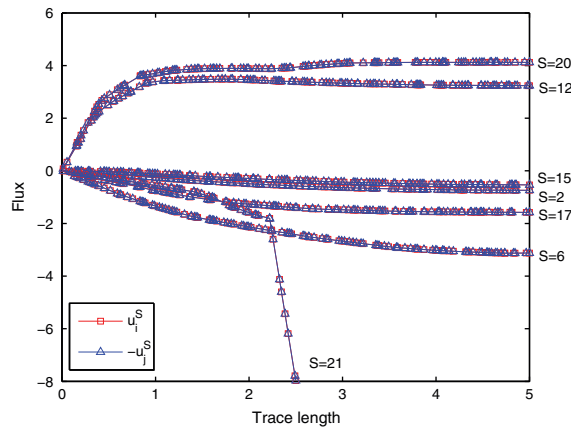

FIG. 5.21. *Problem* 11F: *Solution* u_i *on the traces of fracture* F_6 *and solutions* $\{-u_j\}$ *on the fractures intersecting* F_6 *in its traces.*
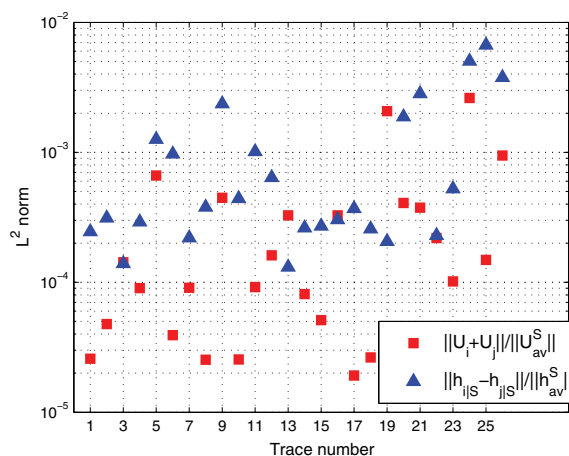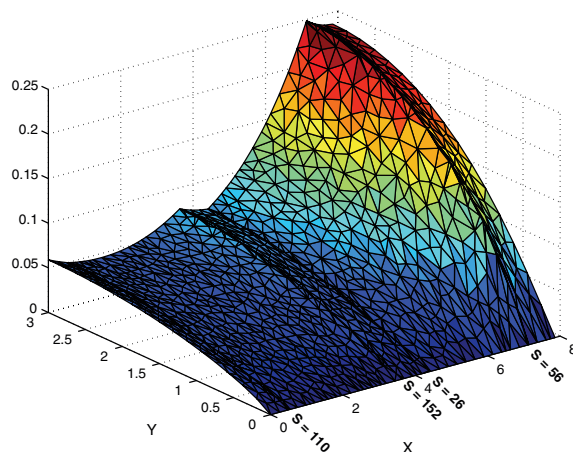
FIG. 5.22. *Problem* 11F: *relative continuity mismatch and flux unbalance.*

FIG. 5.23. *Problem* 50F: *Solution on fracture* F_{50} *(traces numbering is global).*

reported here are obtained with a grid parameter $\delta_{\max} = 0.16$. As shown in particular in the two-dimensional plots, the computed numerical solution well approximates continuity and flux conservation (2.2)–(2.3). Focusing on the intermediate 11F case, in Figure 5.22 we plot for each trace the L^2-norm of the difference of the hydraulic head on intersecting fractures, $||h_{i|S} - h_{j|S}||$, relative to the average L^2-norm of h on the trace, $h_{av} = 1/2(||h_{i|S}|| + ||h_{j|S}||)$ (triangular markers), and in square markers flux unbalance at traces, $||u_i + u_j||$, relative to the average flux $u_{av} = 1/2\left(||u_i|| + ||u_j||\right)$. It can be seen that the relative mismatches in flux conservation and head continuity are small and roughly of the same order. Furthermore, in Table 5.2 we report, again for problem 11F, the flux unbalance and the total flux on each fracture, which are computed on F_i, $i = 1, \ldots, 11$, as $\sum_{S \in \mathcal{S}_i} \int_S u_i^S + u_j^S \, \mathrm{d}\gamma$ and $\sum_{S \in \mathcal{S}_i} \int_S u_i^S \, \mathrm{d}\gamma$, respectively. The sum of the flux unbalances on all the DFN is $-5.0114\mathrm{e}\text{-}7$, and clearly the sum of the total fluxes on the fractures exactly matches this value. It can be seen from the table that flux unbalance on the fractures is quite small, being six orders of magnitude below the respective total flux.
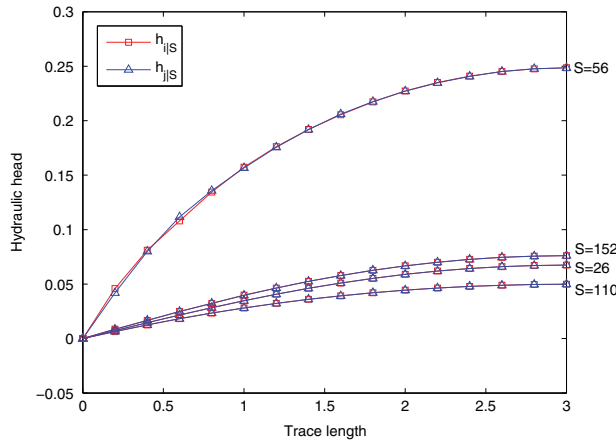
FIG. 5.24. *Problem* 50F: *Solution* h_i *on the traces of fracture* F_{50} *and solutions* $\{h_j\}$ *on the fractures intersecting* F_{50} *in its traces.*
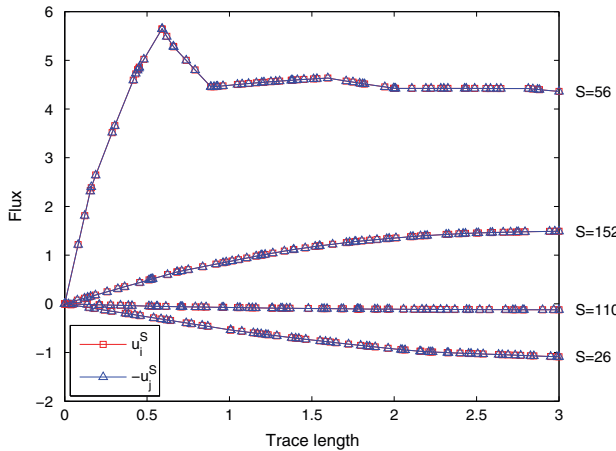

FIG. 5.25. *Problem* 50F: *Solution* u_i *on the traces of fracture* F_{50} *and solutions* $\{-u_j\}$ *on the fractures intersecting* F_{50} *in its traces.*

TABLE 5.2
Problem 11F: *Fracture flux unbalance and total fluxes* ($\delta_{\max} = 0.16$).

	Flux unbalance	Total flux		Flux unbalance	Total flux
F_1	-9.69e-7	1.44	F_7	-1.38e-6	0.50
F_2	-1.98e-6	4.72	F_8	-1.98e-6	-14.41
F_3	2.02e-7	-17.10	F_9	2.19e-6	9.06
F_4	-1.07e-6	2.99	F_{10}	3.61e-6	-4.17
F_5	-9.81e-7	7.20	F_{11}	3.87e-6	2.88
F_6	-2.51e-6	6.87			

5.4. Preconditioning. The choice of a good preconditioner for SYMMLQ is a crucial task as the linear systems arising from the discrete DFN-like problems are ill-conditioned even for the smaller problems considered, and conditioning worsens both if grid parameter is reduced and if the number of fractures increases. In Table 5.3

TABLE 5.3

System matrices data. Dim*: matrix dimension;* NCond*: matrix condition number;* Iter*: iterative solver number of iterations;* Relres*: solution relative residual.*

Problem	Dim	NCond	SYMMLQ Iter	Relres	Grid Prameter
S1	8324	$1.9 \cdot 10^6$	3000	$1.75 \cdot 10^{-1}$	0.1
S2	15067	$9.0 \cdot 10^9$	3000	$1.25 \cdot 10^{-1}$	0.1
7F	18261	$1.3 \cdot 10^9$	3000	1	0.16
11F	32888	$1.7 \cdot 10^{10}$	3000	1	0.16
50F	69476	$9.3 \cdot 10^9$	3000	1	0.22

we report the data related to the conditioning of the system for various problems considered, along with the results obtained while attempting to solve the nonpreconditioned linear system with SYMMLQ. Problems 7F, 11F, and 50F refer to the examples shown in subsection 5.3, while Problems S1 and S2 are a modified version of Problems 7F and 11F, respectively. With reference to Figures 5.12 and 5.13, z-quotes are reduced in Problems S1 and S2 to $z = 1$ for the fractures represented with solid lines and to $z = 0.5$ for the fracture shown by dashed line. Different Dirichlet boundary conditions are set on fracture edges in the z-direction marked with a black dot, while homogeneous Dirichlet boundary conditions are placed on the remaining edges. Finally a constant value $K = 1$ is prescribed to all the fractures. These modified problems yield smaller linear systems. The data in Table 5.3 show that the iterative solver never succeeded in reaching the required exit tolerance $tol = 10^{-6}$ within the maximum number of iterations allowed ($\max_{it} = 3000$).

In order to precondition the system, we follow here the approach described in [27], in which a block triangular preconditioner is suggested for linear systems of saddle point type arising from general quadratic programming problems. In detail, for a saddle point problem of the form (3.6), the following preconditioner is suggested:

$$(5.1) \qquad \mathcal{P} = \begin{pmatrix} G + C^T W^{-1} C & kC^T \\ 0 & W \end{pmatrix},$$

where k is a scalar and W is an $N^F \times N^F$ symmetric positive definite weight matrix. A suitable choice for k and W suggested in [27] is $k = 0$ and $W = \gamma I$, where I is the identity matrix and $\gamma > 0$ is a given constant which should provide an augmenting term $C^T W^{-1} C$ not too small in comparison with G. We remark that the choice $k = 0$ yields a block diagonal symmetric preconditioner and hence is suitable for use along with the SYMMLQ solver.

The preconditioner (5.1) is introduced in [27] in the context of interior point methods for optimization problems, which especially in the case of inexact methods [2] heavily rely on iterative methods and hence on good preconditioners. In the case of interior point methods, at each outer iteration a linear system with a structure similar to (3.6) has to be solved with the block G being typically more and more ill-conditioned as the solution is approached. In [27], an adaptive choice of γ along outer iterations appears to be an effective choice: when used in conjunction with the MINRES solver, an effective choice is $\gamma = 1/\max(G)$ for linear programming problems, and for quadratic programming problems the choice suggested is given by $\gamma = \|C\|^2/\|G\|$.

Since here we deal with a different context and the block G is not necessarily the major source of ill-conditioning, a preliminary investigation has been performed on Problems S1, S2, 7F, 11F, and 50F in order to study the effectiveness of the preconditioner in our applications and, possibly, identify a suitable value for the parameter
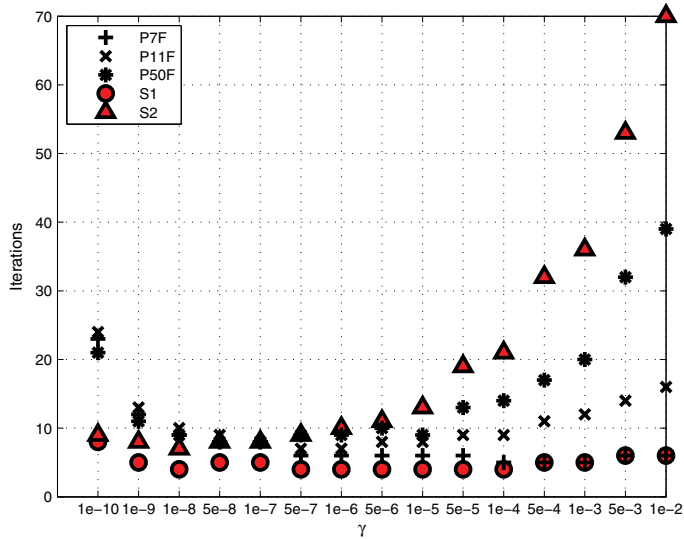
FIG. 5.26. *SYMMLQ number of iterations versus γ.*

γ. A broad range of values for γ has been considered, ranging between 10^{-9} and 300, which roughly corresponds to the optimal value $\|C\|^2/\|G\|$ suggested in [27] applied to problems S1 and S2. For problems 7F, 11F, and 50F this value corresponds to $\approx 7 \cdot 10^5$. Exit tolerance for the iterative solver is now set to $tol = 10^{-12}$ and the maximum number of iterations is set to $\max_{it} = 3000$. We point out that the implementation of SYMMLQ that we used for solving the system $\mathcal{A}x = q$ performs the check on the exit tolerance on the unpreconditioned relative residual $\|q - \mathcal{A}x\|/\|q\|$ even if the linear system is preconditioned. Results of this preliminary investigation are reported in Figures 5.26 and 5.27. In particular, in Figure 5.26 we report the number of iterations required by SYMMLQ for several values of γ. As shown in the figure, in all problems considered for γ small enough the iterative solver succeeded in satisfying the stopping criterion within a very moderate number of iterations. The value $γ = 10^{-7}$ appears to ensure the best performance in the preconditioner for all the considered problems, independently of the number of fractures, of the number of unknowns and of the boundary conditions. Indeed, Figure 5.27 shows that for optimal
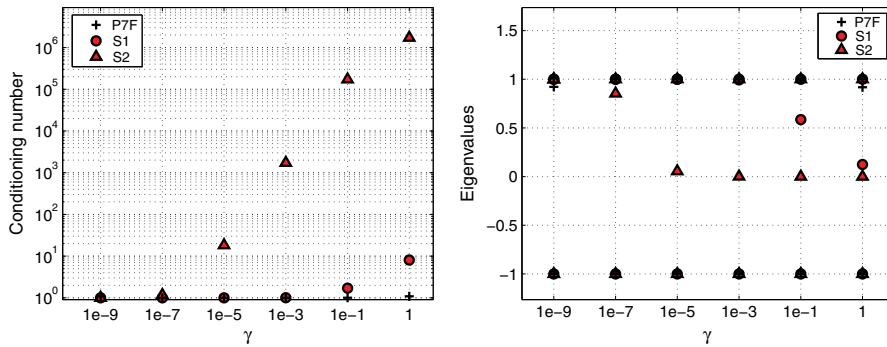

FIG. 5.27. *Preconditioned system: condition number (left) and eigenvalues (right) versus γ.*

γ values the condition number of the preconditioned linear system reaches very low values and matrix eigenvalues cluster around the values $\{-1, 1\}$.

5.5. Large variation of K values. In previous computations we allowed a different transmissivity value K_i on each fracture F_i, $i \in \mathfrak{I}$ (assuming for simplicity K_i constant on the fracture). In real applications, large variations in the (typically very small) values of K_i may occur from fracture to fracture, possibly spanning several orders of magnitude. This may correspondingly cause a large variation in the orders of magnitude of U, which, representing the conormal derivative $n^T K \nabla H$, may largely differ from those of H, making the functional J less sensitive to variation in U. In order to deal with this situation, a possible approach consists in properly weighting the terms $\|U_i^S + U_j^S\|$ in the functional, allowing the following modification to J:

$$J(U) = \sum_{S \in \mathcal{S}} J^S(U) = \sum_{S \in \mathcal{S}} \left(\|C_i^S H_i(U_i) - C_j^S H_j(U_j)\|_{\mathcal{H}^S}^2 + \frac{1}{(K_{\min}^S)^\alpha} \|U_i^S + U_j^S\|_{\mathcal{U}^S}^2 \right),$$

where $K_{\min}^S = \min\{K_i, K_j\}$ and, e.g., $\alpha = 1, 2$. The weights introduced help in balancing the contribution of the various terms of the cost functional, giving more relevance to flux unbalance when large variations of transmissivity occur at intersecting fractures. The following model problem has been used to show the effectiveness of this extension of the method, here applied with $\alpha = 1$. The problem domain is shown on the left of Figure 5.28, along with fracture and trace numbering. Fracture F_1 carries a constant value Dirichelet boundary condition $h = 10$ on the top border along the y-axis, while fracture F_3 has a Dirichelet boundary condition $h = 3$ on the bottom border parallel to the y-axis. Fractures F_2 and F_4 have a constant value $h = 1$ Dirichelet boundary condition on the left border parallel to the y-axis. A homogeneous Neumann boundary condition is prescribed on the remaining borders of all fractures. Four different simulations are performed with different sets of fracture transmissivity values as reported on the right of Figure 5.28. It was noted that with these broad variations of K, the correction helped in obtaining the solution, as we experienced difficulties in convergence of the steepest descent method with the nonmodified functional. Results concerning hydraulic head mismatch at traces and flux unbalance are collected in Figures 5.29 and 5.30. In Figure 5.29 the $L^2(S)$-norm of the difference of the hydraulic head on intersecting fractures $E_h = \|h_{i|S} - h_{j|S}\|$ is reported with solid markers for each trace, along with the average $L^2(S)$-norm of h,
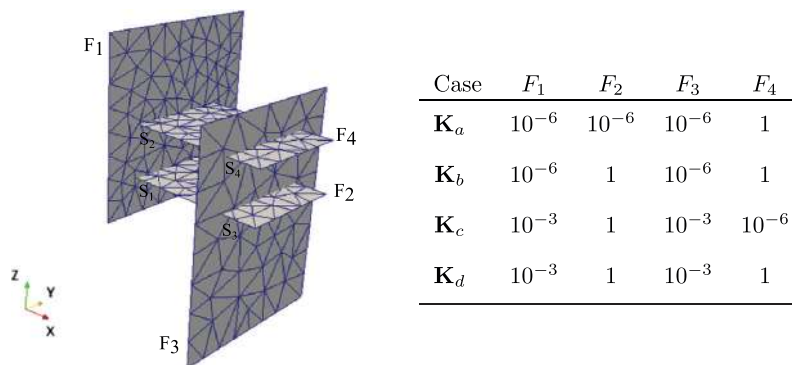

Case	F_1	F_2	F_3	F_4
$\mathbf{K}_a$	10^{-6}	10^{-6}	10^{-6}	1
$\mathbf{K}_b$	10^{-6}	1	10^{-6}	1
$\mathbf{K}_c$	10^{-3}	1	10^{-3}	10^{-6}
$\mathbf{K}_d$	10^{-3}	1	10^{-3}	1

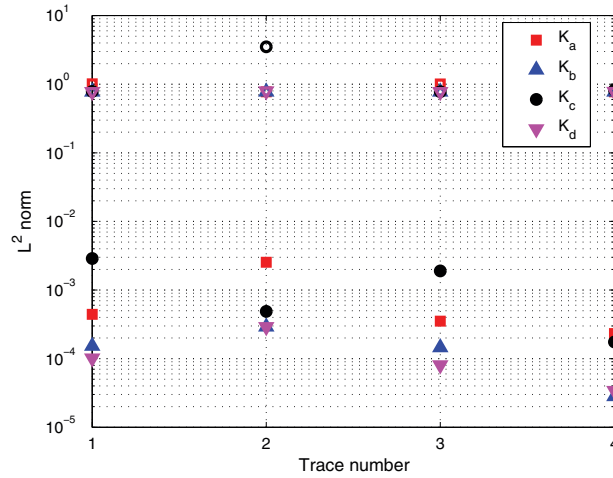FIG. 5.28. *Domain description and fracture transmissivity values.*

FIG. 5.29. L^2-norm of hydraulic head mismatch E_h (filled markers) and average L^2-norm of solution h_{av} (empty markers) on the traces of the system.
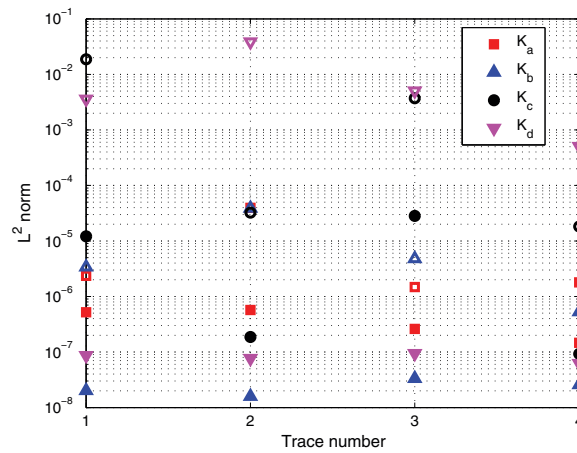

FIG. 5.30. L^2-norm of flux unbalance E_u (filled markers) and average L^2-norm of fluxes u_{av} (empty markers) on the traces of the system.

$h_{av} = 1/2(||h_{i|S}|| + ||h_{j|S}||)$ (in empty markers) in order to compare the mismatch of h at the intersections in relation to the order of magnitude of the solution. Similarly, in Figure 5.30 we show flux unbalance at traces in solid markers, $E_u = ||u_i + u_j||$, with the average flux $u_{av} = 1/2(||u_i|| + ||u_j||)$ in empty markers. It is noticed that the hydraulic head mismatch on traces and the flux unbalance are usually orders of magnitude lower than the hydraulic head and the flux, respectively, also for fracture transmissivities differing for six orders of magnitude.

6. Conclusions. In this paper we have further analyzed the viability in complex systems of a novel method introduced in [6] for the problem of subsurface flow in a system of fractures, which consists in the reformulation of the problem as a PDE constrained optimization problem. Independent meshing processes have been used on the fractures, generating grids which are independent of the mesh on other fractures and of trace number and disposition. This is a crucial point since one of major

difficulties in the DFN approach is typically the generation of a trace-matching mesh. The discussion and the experiments reported here show effectiveness of the method in providing good approximation of the solution in complex DFNs.

In future works, more realistic DFN configurations will be investigated. A parallel implementation exploiting the independence of the problems on the subfractures is also envisaged. Moreover, we will investigate the applicability of the method to the non-steady-state case in conjunction with local time adaptive strategies as in [7].

REFERENCES

[1] I. BABUŠKA AND J. M. MELENK, *The partition of unity method*, Internat. J. Numer. Methods Engrg., 40 (1997), pp. 727–758.

[2] S. BELLAVIA AND S. PIERACCINI, *Convergence analysis of an inexact infeasible interior point method for semidefinite programming*, Comput. Optim. Appl., 29 (2004), pp. 289–313.

[3] T. BELYTSCHKO AND T. BLACK, *Elastic crack growth in finite elements with minimal remeshing*, Internat. J. Numer. Methods Engrg., 45 (1999), pp. 601–620.

[4] T. BELYTSCHKO, N. MÖES, S. USUI, AND C. PARIMI, *Arbitrary discontinuities in finite elements*, Internat. J. Numer. Methods Engrg., 50 (2001), pp. 993–1013.

[5] M. BENZI, G. H. GOLUB, AND J. LIESEN, *Numerical solution of saddle point problems*, Acta Numer., 14 (2005), pp. 1–137.

[6] S. BERRONE, S. PIERACCINI, AND S. SCIALÒ, *A PDE-constrained optimization formulation for discrete fracture network flows,* SIAM J. Sci. Comput., 35 (2013), pp. B487–B510.

[7] S. BERRONE, *A local-in-space-timestep approach to a finite element discretization of the heat equation with a posteriori estimates*, SIAM J. Numer. Anal., 47 (2009), pp. 3109–3138.

[8] M. C. CACAS, E. LEDOUX, G. DE MARSILY, B. TILLIE, A. BARBREAU, E. DURAND, B. FEUGA, AND P. PEAUDECERF, *Modeling fracture flow with a stochastic discrete fracture network: Calibration and validation: 1. The flow model*, Water Resource Res., 26 (1990), pp. 479–489.

[9] J. CHESSA, H. WANG, AND T. BELYTSCHKO, *On the construction of blending elements for local partition of unity enriched finite elements*, Internat. J. Numer. Methods Engrg., 57 (2003), pp. 1015–1038.

[10] C. D'ANGELO AND A. SCOTTI, *A mixed finite element method for Darcy flow in fractured porous media with non-matching grids*, ESAIM Math. Model. Numer. Anal., 46 (2012), pp. 465–489.

[11] C. DAUX, N. MÖES, J. DOLBOW, N. SUKUMAR, AND T. BELYTSCHKO, *Arbitrary branched and intersecting cracks with the extended finite element method*, Internat. J. Numer. Methods Engrg., 48 (2000), pp. 1741–1760.

[12] W. S. DERSHOWITZ AND H. H. EINSTEIN, *Characterizing rock joint geometry with joint system models*, Rock Mechanics and Rock Engineering, 1 (1988), pp. 21–51.

[13] W. S. DERSHOWITZ AND C. FIDELIBUS, *Derivation of equivalent pipe networks analogues for three-dimensional discrete fracture networks by the boundary element method*, Water Resource Res., 35 (1999), pp. 2685–2691.

[14] J.-R. DE DREUZY, G. PICHOT, B. POIRRIEZ, AND J. ERHEL, *Synthetic benchmark for modeling flow in* 3D *fractured media*, Comput. Geosci., 50 (2013), pp. 59–71.

[15] J. ERHEL, J.-R. DE DREUZY, AND B. POIRRIEZ, *Flow simulation in three-dimensional discrete fracture networks*, SIAM J. Sci. Comput., 31 (2009), pp. 2688–2705.

[16] T.-P. FRIES AND T. BELYTSCHKO, *The extended/generalized finite element method: An overview of the method and its applications*, Internat. J. Numer. Methods Engrg., 84 (2010), pp. 253–304.

[17] T.-P. FRIES, *A corrected XFEM approximation without problems in blending elements*, Internat. J. Numer. Methods Engrg., 75 (2008), pp. 503–532.

[18] T. KALBACHER, R. METTIER, C. MCDERMOTT, W. WANG, G. KOSAKOWSKI, T. TANIGUCHI, AND O. KOLDITZ, *Geometric modelling and object-oriented software concepts applied to a heterogeneous fractured network from the grimsel rock laboratory*, Comput. Geosci., 11 (2007), pp. 9–26.

[19] P. LABORDE, J. POMMIER, Y. RENARD, AND M. SALAÜN, *High-order extended finite element method for cracked domains*, Internat. J. Numer. Methods Engrg., 64 (2005), pp. 354–381.

[20] N. MÖES, J. DOLBOW, AND T. BELYTSCHKO, *A finite element method for crack growth without remeshing*, Internat. J. Numer. Methods Engrg., 46 (1999), pp. 131–150.

[21] H. Mustapha and K. Mustapha, *A new approach to simulating flow in discrete fracture networks with an optimized mesh*, SIAM J. Sci. Comput., 29 (2007), pp. 1439–1459.

[22] J. Nocedal and S. Wright, *Numerical Optimization*, Springer, New York, 1999.

[23] A. W. Nordqvist, Y. W. Tsang, C. F. Tsang, B. Dverstop, and J. Andersson, *A variable aperture fracture network model for flow and transport in fractured rocks*, Water Resource Res., 28 (1992), pp. 1703–1713.

[24] C. C. Paige and M. A. Saunders, *Solution of sparse indefinite systems of linear equations*, SIAM J. Numer. Anal., 12 (1975), pp. 617–629.

[25] G. Pichot, J. Erhel, and J.-R. De Dreuzy, *A mixed hybrid Mortar method for solving flow in discrete fracture networks*, Appl. Anal., 89 (2010), pp. 1629–1643.

[26] G. Pichot, J. Erhel, and J.-R. de Dreuzy, *A generalized mixed hybrid mortar method for solving flow in stochastic discrete fracture networks*, SIAM J. Sci. Comput., 34 (2012), pp. B86–B105.

[27] T. Rees and C. Greif, *A preconditioner for linear systems arising from interior point optimization methods*, SIAM J. Sci. Comput., 29 (2007), pp. 1992–2007.

[28] J. R. Shewchuk, *Delaunay refinement algorithms for triangular mesh generation*, Comput. Geom., 22 (2002), pp. 21–74.

[29] N. Sukumar, D. Chopp, N. Möes, and T. Belytschko, *Modeling holes and inclusions by level sets in the extended finite element method*, Comput. Methods Appl. Mech. Engrg., 190 (2001), pp. 1209–1233.

[30] M. Vohralík, J. Maryška, and O. Severýn, *Mixed and nonconforming finite element methods on a system of polygons*, Appl. Numer. Math., 51 (2007), pp. 176–193.